

# Observation of Low Energy Raman Modes in Twisted Bilayer Graphene

Rui He,<sup>\*,†,¶</sup> Ting-Fung Chung,<sup>‡,§,¶</sup> Conor Delaney,<sup>†</sup> Courtney Keiser,<sup>†</sup> Luis A. Jauregui,<sup>§,||</sup> Paul M. Shand,<sup>†</sup> C. C. Chancey,<sup>†</sup> Yanan Wang,<sup>⊥</sup> Jiming Bao,<sup>⊥</sup> and Yong P. Chen<sup>\*,‡,§,||</sup>

<sup>†</sup>Department of Physics, University of Northern Iowa, Cedar Falls, Iowa 50614, United States

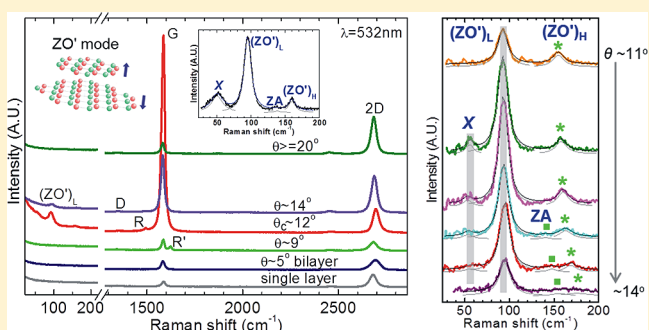
<sup>‡</sup>Department of Physics, <sup>§</sup>Birck Nanotechnology Center, and <sup>||</sup>School of Electrical and Computer Engineering, Purdue University, West Lafayette, Indiana 47907, United States

<sup>⊥</sup>Department of Electrical and Computer Engineering, University of Houston, Houston, Texas 77204, United States

**S** Supporting Information

**ABSTRACT:** Two new Raman modes below  $100\text{ cm}^{-1}$  are observed in twisted bilayer graphene grown by chemical vapor deposition. The two modes are observed in a small range of twisting angle at which the intensity of the G Raman peak is strongly enhanced, indicating that these low energy modes and the G Raman mode share the same resonance enhancement mechanism, as a function of twisting angle. The  $\sim 94\text{ cm}^{-1}$  mode (measured with a 532 nm laser excitation) is assigned to the fundamental layer breathing vibration (ZO' mode) mediated by the twisted bilayer graphene lattice, which lacks long-range translational symmetry. The dependence of this mode's frequency and line width on the rotational angle can be explained by the double resonance Raman process that is different from the previously identified Raman processes activated by twisted bilayer graphene superlattice. The dependence also reveals the strong impact of electronic-band overlaps of the two graphene layers. Another new mode at  $\sim 52\text{ cm}^{-1}$ , not observed previously in the bilayer graphene system, is tentatively attributed to a torsion mode in which the bottom and top graphene layers rotate out-of-phase in the plane.

**KEYWORDS:** Bilayer graphene, twisted, Raman, low energy modes



In bilayer graphene (BLG) exfoliated from highly oriented pyrolytic graphite (HOPG) crystals, the top and bottom graphene layers usually form Bernal (A-B) stacking in which the carbon atoms of the B sublattice of the second layer sit on top of the A sublattice carbon atoms of the first graphene layer. Two parallel parabolic conduction bands situated above another two parallel parabolic valence bands with zero bandgap characterizes the low energy (near the charge neutral point) electronic band structure of Bernal-stacked BLG.<sup>1–3</sup> However, in twisted BLG (tBLG) in which the second graphene layer is rotated with respect to the first layer, the low-energy electronic band structure can be represented by two Dirac cones separated by a wavevector that depends on the rotational angle.<sup>4,5</sup> While linear dispersion is maintained in tBLG system, van Hove singularities in the density of states (DOS) are generated due to the coupling of the two layers.<sup>4</sup> In addition, tBLG exhibits interesting optical features with optical absorption bands in the visible range.<sup>6,7</sup> Hence, probing the fundamental properties of tBLG is of interest and importance.

Phonons play an important role in electron transport in BLG through electron–phonon interactions.<sup>8</sup> Low energy phonons, for example, the layer breathing mode in which the two graphene layers vibrate out-of-phase perpendicular to their

planes, facilitate interlayer current conduction in tBLG.<sup>9</sup> Raman spectroscopy is a noninvasive, direct, and sensitive probe of phonons in graphene layers. It has been shown that the intensity of the G Raman peak and the position, line width, and intensity of the 2D Raman band undergo characteristic changes as a function of twisting angle.<sup>4,5</sup> In addition, new Raman lines, for example, R and R' peaks close to the G band, other lines around the D peak, and out-of-plane acoustic (ZA) and layer breathing (ZO') modes (between  $120$  and  $200\text{ cm}^{-1}$ ) are observed in tBLG due to Raman processes in which finite wavevector phonon scatterings are activated by involving angle dependent superlattice wavevectors.<sup>10–12</sup>

In this paper, we report the observation of new low energy vibrational modes below  $100\text{ cm}^{-1}$  in Raman scattering from tBLG. For a given laser excitation energy, these modes are only observed in the vicinity of a specific twisting angle at which the G Raman band is strongly enhanced. This observation indicates that the resonance enhancement mechanism of the low energy modes is similar to that of the G band enhancement.<sup>4,5</sup> In

**Received:** April 15, 2013

**Revised:** July 12, 2013

**Published:** July 16, 2013

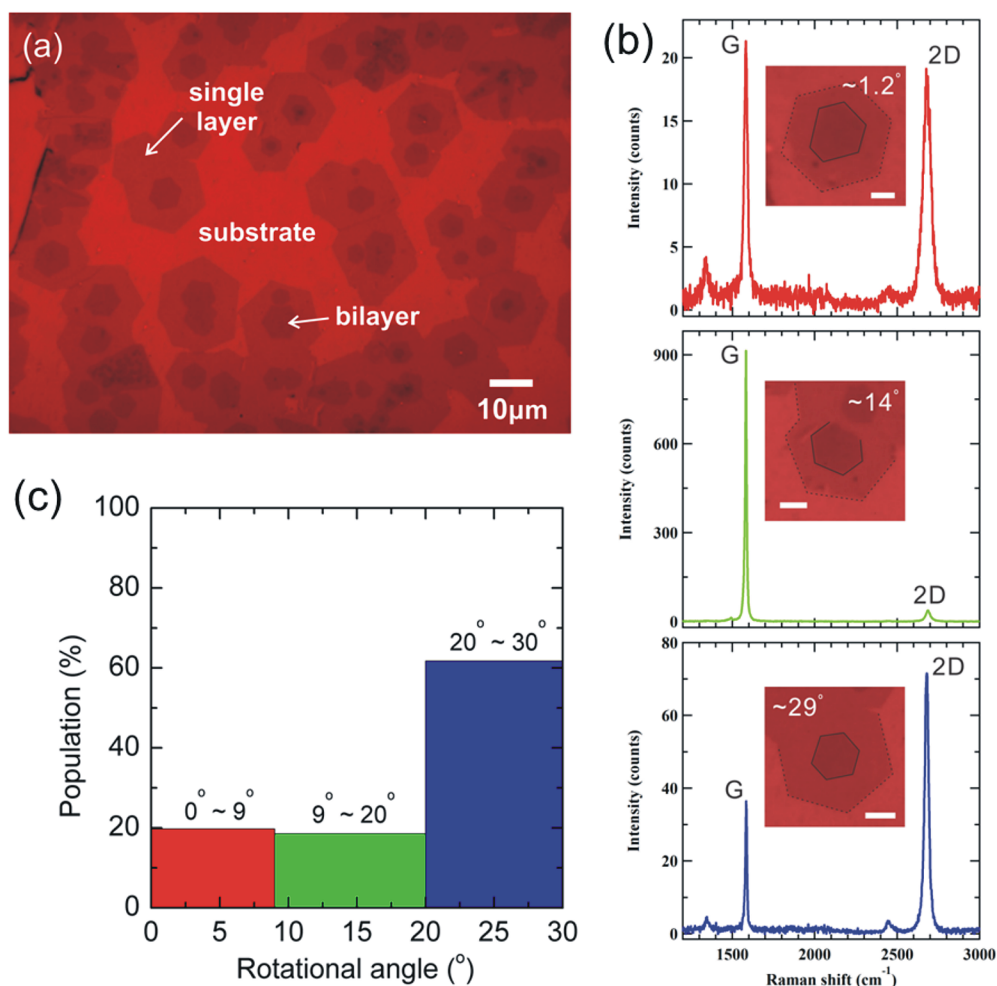


**Figure 1.** An example of twisted bilayer graphene (tBLG) domains grown by APCVD. (a) Optical image of tBLG domains transferred onto Si substrate with  $\sim 300$  nm thermal oxide. The domains mostly have a hexagonal shape with edges parallel to zigzag directions.<sup>17</sup> (b) Representative Raman spectra and optical images of BLG domains with low, intermediate (near the critical angle where G peak intensity shows a resonance enhancement), and high twisting angles. The larger hexagonal first layer domains are highlighted by dashed lines, and the smaller hexagonal second layer domains are delineated by black solid lines for clarity. All Raman measurements were conducted at room temperature using a 532 nm laser excitation. The scale bars in optical images of tBLG domains with twisting angles of  $\sim 1.2^\circ$ ,  $\sim 14^\circ$ , and  $\sim 29^\circ$  are 2, 3, and 5  $\mu\text{m}$ , respectively. (c) Histogram of twisting angles of BLG domains in our CVD graphene sample determined by G and 2D Raman features. The histogram is based on a total of 81 BLG domains.

addition to the resonance enhancement of the intensities of the observed low energy Raman modes, the intensity of the background on which the low energy Raman peaks are superimposed is also enhanced near the critical twisting angle. This broad and enhanced background at low energy could be related to electronic excitations in tBLG. The Raman peak at  $\sim 94$   $\text{cm}^{-1}$  (measured with laser wavelength 532 nm), referred to as  $(\text{ZO}')_{\text{L}}$  mode in this paper, is assigned to the fundamental layer breathing mode (arising from the out-of-plane relative motions of the two graphene layers). This mode can be explained by the double resonance mechanism and may be activated by the tBLG lattice that lacks long-range translational symmetry. The dependence of the frequency and line width of this mode on the twisting angle reveals the degree of overlap of the two Dirac cones that belong to the two layers in tBLG. This fundamental  $\text{ZO}'$  mode is also observed at a higher frequency above 100  $\text{cm}^{-1}$  (here referred to as  $(\text{ZO}')_{\text{H}}$ ) and is understood to be mediated by the tBLG superlattice with wavevector  $\mathbf{q}$ .<sup>13</sup> The coexistence of two fundamental  $\text{ZO}'$  Raman lines originating from phonons in different parts of the

Brillouin zone (with different phonon wavevectors) suggests that although the tBLG system lacks long-range translational symmetry, superlattice periodicity can still be defined. In contrast, in Bernal-stacked BLG, the fundamental layer breathing ( $\text{ZO}'$ ) mode is known to be spectroscopically inactive (silent) and has never been observed previously (only its overtone  $2\text{ZO}'$  was observed).<sup>14,15</sup> Our observation indicates that tBLG differs dramatically from Bernal-stacked BLG and highlights that tBLG is a very interesting system that allows us to probe a broad range of phonon dispersion in the interior of the Brillouin zone. Another mode at  $\sim 52$   $\text{cm}^{-1}$  is tentatively assigned to a torsion mode that also appears to be activated in the tBLG system but not in the Bernal-stacked BLG.

Our graphene layers were grown by chemical vapor deposition (CVD) on Cu foils at ambient pressure<sup>16,17</sup> (APCVD) and transferred onto a highly p-doped Si substrate (with  $\sim 300$  nm  $\text{SiO}_2$ ) for all subsequent measurements. Details of the sample growth are shown in the Supporting Information. Figure 1a shows an optical image of CVD graphene on Si/ $\text{SiO}_2$

substrate. Single layer and bilayer graphene areas can be identified from the color contrast. It is seen that  $\sim 70$ – $80\%$  of the substrate is covered by graphene (polycrystalline consisting of single crystal graphene domains). The first layer domains have a typical size of  $\sim 20 \mu\text{m}$  and largely connect with neighboring domains. The second layer domains are often located near the centers of the first layer domains and have a typical lateral size of a few micrometers. The graphene domains grown by our CVD method are mostly hexagonal in shape with edges parallel to zigzag directions of the graphene lattice<sup>17</sup> (thus facilitating the determination of the lattice orientation using these edges; see below). The number of layers is confirmed by both Raman measurements as well as by measurements of the thickness of bilayer domains by atomic force microscopy (AFM) in a tapping mode (see a representative AFM image in the Supporting Information).

Figure 1b illustrates three representative Raman spectra measured from tBLG domains with different twisting angles. From the G and 2D Raman band features,<sup>4,5</sup> we can estimate the twisting angles. The insets display the corresponding optical images of each BLG domain. Contours of the single-layer (dashed lines) and bilayer (solid lines) areas have been included as guides to the eye. The twisting (misorientation) angles can also be determined by measuring the angles formed between neighboring edges of the first and the second layer domains.<sup>18</sup> Both methods provide consistent estimation of twisting angles (within  $\sim 2^\circ$ ). Figure 1c summarizes the distribution of twisting angles determined by the Raman method. A similar histogram of BLG twisting angles is also obtained by measuring the relative orientations between the edges of top and bottom graphene layers seen in optical images (see the Supporting Information). The twisting angle distribution suggests that our APCVD growth favors tBLG with a large twisting angle ( $20$ – $30^\circ$ ). This is very different from the bilayer domains grown by low-pressure (LP) CVD that are largely in Bernal-stacked configuration (no-twisting).<sup>19,20</sup> This finding reveals that the distribution of rotational angles in tBLG depends on the growth conditions, which influence the growth kinetics of CVD graphene.

Figure 2a shows five representative Raman spectra measured down to low Raman shifts ( $<100 \text{ cm}^{-1}$ ) from our probes of five different bilayer domains. A spectrum from single layer graphene (SLG) is included for comparison. From the positions, linewidths, and intensities of the R, G, and 2D Raman bands, we can approximately determine the twisting angles in these bilayer domains (labeled in Figure 2a). For 532 nm laser excitation, the G peak intensity reaches maximum and concomitantly the 2D band exhibits the greatest blueshift from that of the SLG when the twisting angle  $\theta$  is near the critical twisting angle  $\theta_c = 12^\circ$  (see the red spectrum in Figure 2a).<sup>5</sup> Qualitatively similar phenomena are seen for the 633 nm laser excitation (see the Supporting Information). The critical angle  $\theta_c$  varies for different laser excitation energies.<sup>4</sup> This is shown by different intensities in Raman mapping over the same tBLG island by using different laser excitation energies<sup>21</sup> (also see the Supporting Information). All Raman data shown in the main text are measured with a 532 nm laser excitation unless otherwise stated. The D peak intensity is very low or negligible in most bilayer domains that we studied. This implies that the quality of the graphene layers is high. In addition to the G and 2D peaks, several low energy Raman modes and a strong background on which the low energy Raman modes superimpose are observed when the twisting angle is in the vicinity of

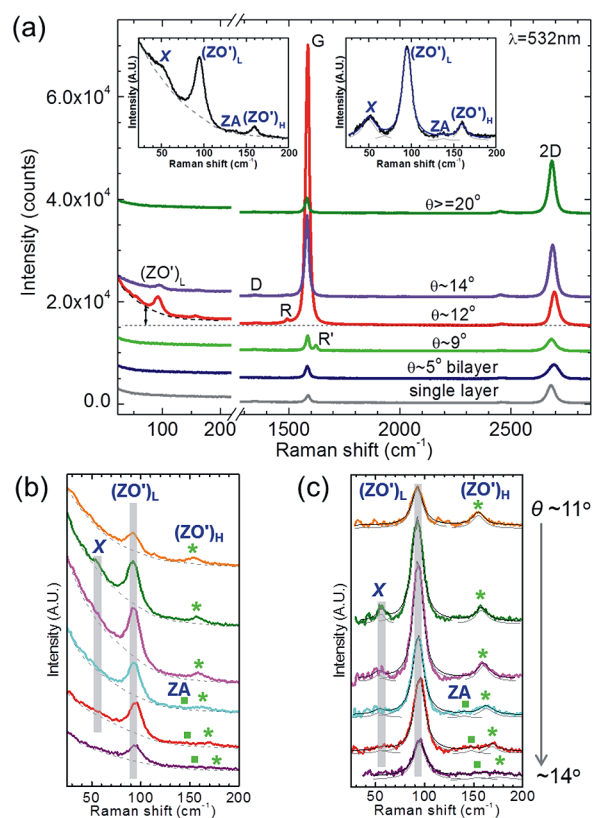


**Figure 2.** (a) Raman spectra from tBLG domains with different twisting angle  $\theta$ . A spectrum from SLG is included for comparison. The vertical scale is the same before and after the break on the horizontal axis. We define the low-energy background intensity to be the height intensity of the envelope (at  $70 \text{ cm}^{-1}$ ) on which the low-energy Raman peaks superimpose (shown by the black vertical arrow for the spectrum with  $\theta \sim 12^\circ$ ). The left inset displays a zoomed-in low-energy spectrum. The right inset displays the same spectrum after subtraction of the background envelope highlighted by the dashed line shown in the left inset. The spectrum is decomposed into up to four Lorentzian peaks. (b,c) Original and background-subtracted low-energy Raman spectra from six different bilayer domains with twisting angles in the vicinity of  $\theta_c$ . Full spectra including the R, G, and 2D bands are shown in the Supporting Information. On the basis of the R peak position, we determine that the twisting angle  $\theta$  varies from  $\sim 11$  to  $\sim 14^\circ$ . In panel (c), the gray vertical bars highlight X and  $(\text{ZO}')_L$  modes. The squares and asterisks highlight ZA and  $(\text{ZO}')_H$  modes, respectively. All spectra are excited by a 532 nm laser excitation.

$\theta_c$ . A representative zoomed-in low-energy spectrum is shown in the left inset of Figure 2a. The inset on the right-hand side shows the same spectrum after subtracting the background (highlighted by the dashed line in the left inset). Four Raman modes (as shown by four Lorentzian peaks after the spectrum is decomposed) are observed within the range of  $30$ – $200 \text{ cm}^{-1}$ . These low energy Raman features, particularly the two newly observed modes below  $100 \text{ cm}^{-1}$ , are the main focus of this paper.

Dispersion of low-energy phonons in tBLG has not been well-explored thus far. Theoretical calculation of dispersion curves of low-energy phonons of the tBLG system is very challenging since the unit cell size required is very large. Only limited experimental work of low energy phonons (in the range  $100$ – $200 \text{ cm}^{-1}$ ) and dispersions has been reported in the literature.<sup>13</sup> These phonons of above  $100 \text{ cm}^{-1}$  are described by Raman scattering processes mediated by the superlattice

wavevector  $\mathbf{q}$  that depends only on the twisting angle  $\theta$ .<sup>10,13</sup> The frequency–wavevector relation for these phonons overlaps with the SLG and the ZO' (layer breathing mode as schematically shown in Figure 4b) phonon dispersion curves of Bernal-stacked BLG.<sup>13</sup> Figure 5 shows low-frequency (below 200  $\text{cm}^{-1}$ ) phonon dispersion.

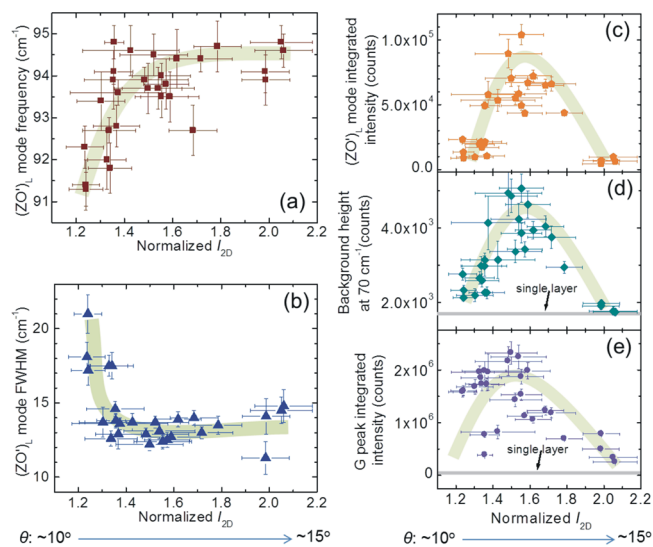
Figure 2b,c shows original and background-subtracted low-energy Raman spectra from several different bilayer domains. From the R, G, and 2D Raman characteristics (spectra are shown in the Supporting Information), we determined that the twisting angles  $\theta$  of these bilayer domains range from  $\sim 11$  ( $< \theta_c$ ) to  $\sim 14^\circ$  ( $> \theta_c$ ). Two modes highlighted by asterisks and squares are observed between 130 and 180  $\text{cm}^{-1}$  (see Figure 2b,c). The frequencies of these two modes blueshift monotonically with the increase of the twisting angle  $\theta$  and agree well with those reported in ref 13. Hence, these modes highlighted by asterisks and squares are attributed to fundamental layer breathing (ZO') and out-of-plane acoustic (ZA) modes, respectively.<sup>13</sup> They are activated by the superlattice (Moire pattern) formed in tBLG.<sup>10</sup> The momentum conservation condition is satisfied by the participation of superlattice wavevector  $\mathbf{q}$  (see Figure 4a). The magnitudes of the scattered phonons thus equal that of the superlattice wavevector  $\mathbf{q}$ , which depends on the twisting angle  $\theta$  and is about  $0.65/0.54 \text{ \AA}^{-1}$  for a twisting angle near  $\theta_c$  ( $\approx 12^\circ/10^\circ$ ) for 532/633 nm laser excitation. The points circled in Figure 5 show the frequencies and wavevectors of these ZO' and ZA phonons activated by the tBLG superlattice as observed in our work.

Figure 2b,c shows that in addition to the modes between 130 and 180  $\text{cm}^{-1}$  two even lower frequency modes are observed. The lowest observed frequency mode (labeled "X") occurs at  $\sim 52 \text{ cm}^{-1}$ . The next higher frequency mode is observed at  $\sim 94 \text{ cm}^{-1}$ , which is close to the frequency of the ZO' mode calculated for and inferred from the observed overtone (2ZO') in Bernal-stacked bilayer graphene.<sup>15,22,23</sup> Hence, we assign this mode to another fundamental layer breathing mode ZO' whose phonon wavevector  $\mathbf{q}'$  is different from the superlattice wavevector  $\mathbf{q}$ . Because this ZO' frequency is lower than that induced by the superlattice, we name this ZO' at 94  $\text{cm}^{-1}$  as (ZO')<sub>L</sub> and the ZO' at higher energy of above 100  $\text{cm}^{-1}$  as (ZO')<sub>H</sub>.

It has been shown by Kim et al. that the integrated intensity of the 2D Raman peak of tBLG increases monotonically with the twisting angle  $\theta$  in the vicinity of  $\theta_c$ .<sup>4</sup> Their studies were conducted on suspended tBLG by consecutively transferring two SLG on a carbon TEM grid where the effects due to the substrates (e.g., doping) are minimized. The same relation between 2D Raman integrated intensity and twisting angle is also observed in our samples (see Figures S2–S4 in the Supporting Information). This suggests it is reasonable to use the integrated intensity of the 2D peak to characterize the twisting angle of our samples. Therefore, we summarize our measurements of the (ZO')<sub>L</sub> mode by plotting the position, bandwidth, and integrated intensities of this mode as a function of normalized 2D Raman intensity ( $I_{2D}$ , normalized to the intensity of SLG, i.e., take the ratio of 2D integrated intensity of BLG to that of the SLG on the sample). Because the G-peak position is sensitive to doping,<sup>8,24</sup> we also plot the G-peak frequency as a function of normalized  $I_{2D}$ . The G-peak frequency vs normalized  $I_{2D}$  plot (see Supporting Information) is very similar to that obtained in suspended tBLG samples reported by Kim et al.<sup>4</sup> This further confirms that doping by the substrate is not a major concern in our studies of the low

energy modes as a function of twisting angle. By comparing the Raman spectra of our SLG domains on the same substrate with previous Raman studies of strained graphene,<sup>25,26</sup> we confirm that strain is not substantial in our samples.

Figure 3a,b displays the evolution of frequency and full width at half-maximum (fwhm) of the (ZO')<sub>L</sub> mode as a function of



**Figure 3.** (a–c) Frequency, fwhm, and integrated intensity of the (ZO')<sub>L</sub> mode as a function of normalized  $I_{2D}$ , respectively. The normalized  $I_{2D}$  is defined as the ratio of the integrated 2D intensity of each bilayer domain to that of a single layer. The data are measured from a series of tBLG domains with twisting angle  $\theta$  ranging from  $\sim 10$  to  $\sim 15^\circ$ , which corresponds to normalized  $I_{2D}$  ranging from 1.1–2.2. (d,e) Background intensity at 70  $\text{cm}^{-1}$  (see Figure 2a and its caption) and integrated intensity of the G peak as a function of the normalized  $I_{2D}$ , respectively. The horizontal lines in these two panels show the respective values of a single layer. The thick curves in each panel are guides to the eye. All results are obtained using a 532 nm laser excitation.

normalized  $I_{2D}$ . The range from 1.1 to 2.2 of the normalized  $I_{2D}$  corresponds to a range of twisting angle  $\theta$  from  $\sim 10$  to  $\sim 15^\circ$ . It is seen that the frequency of this (ZO')<sub>L</sub> mode ( $\omega_{(ZO')_L}$ ) increases with increasing normalized  $I_{2D}$  when the normalized  $I_{2D}$  is below 1.5 (or when  $\theta < 12^\circ$ ).<sup>4</sup> The frequency  $\omega_{(ZO')_L}$  becomes almost constant after the normalized  $I_{2D}$  is greater than 1.5 (or when  $\theta > 12^\circ$ ). Figure 3b shows that the fwhm of the (ZO')<sub>L</sub> mode decreases with increasing normalized  $I_{2D}$  when it is below 1.5 ( $\theta < 12^\circ$ ) and that it also becomes nearly constant when the normalized  $I_{2D}$  is greater than 1.5 ( $\theta > 12^\circ$ ). These results indicate that the dramatic transitions in the frequency and fwhm of the (ZO')<sub>L</sub> mode occur when the twisting angle  $\theta$  is near  $\theta_c$ . In order to confirm the characteristics of the (ZO')<sub>L</sub> mode, we also plot (see Supporting Information) the position and width of this peak as a function of the R mode frequency that decreases monotonically with  $\theta$ .<sup>13</sup> Similar trends as those plotted as a function of normalized  $I_{2D}$  are observed.

The coexistence of two ZO' phonons with different wavevectors is a novel phenomenon. Because the (ZO')<sub>H</sub> phonon's wavevector is defined by the tBLG superlattice, the fundamental (ZO')<sub>L</sub> mode that we observe for the first time in Raman scattering from tBLG must be activated by a different wavevector that satisfies the momentum conservation require-

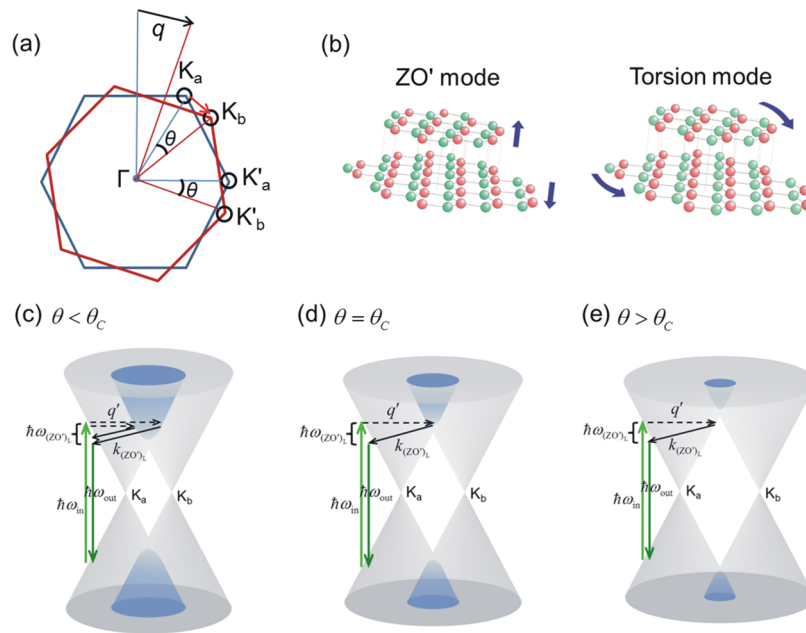


**Figure 4.** (a) The first Brillouin zone in the electronic band structure of tBLG with twisting angle  $\theta$ .  $K_a$  and  $K'_a$  are two adjacent Dirac points of the first graphene layer.  $K_b$  and  $K'_b$  are the two adjacent Dirac points of the second layer.  $q$  is the wavevector of the tBLG superlattice (Moire pattern). (b) Schematic drawings of motions of atoms in the layer breathing ( $ZO'$ ) and torsion ( $X$ ) modes. (c–e) Schematic drawings of Raman processes of ( $ZO'$ )<sub>L</sub> phonon when  $\theta$  is less, equal to, or greater than the critical angle  $\theta_c$ , respectively.  $\hbar\omega_{in}$  is the incident photon energy.  $\hbar\omega_{out}$  is the scattered photon energy.  $\hbar\omega_{(ZO')L}$  is the phonon energy. The dashed arrows show the scattering of electrons by the tBLG crystal lattice. This scattering is elastic and is characterized by the wavevector  $q'$ .  $k_{(ZO')L}$  is the wavevector of the ( $ZO'$ )<sub>L</sub> phonon. The portions of the two Dirac cones (at Dirac points  $K_a$  and  $K_b$ ) that overlap are shown in blue.

ment. We propose that the ( $ZO'$ )<sub>L</sub> mode at  $\sim 94$   $\text{cm}^{-1}$  is facilitated by the tBLG crystal lattice that lacks translational symmetry. The Raman process for this ( $ZO'$ )<sub>L</sub> phonon is an intravalley scattering process<sup>15,23</sup> and involves four steps (see Figure 4c–e): (i) the incident photon creates an electron–hole pair; (ii) the electron/hole is scattered by a tBLG crystal lattice (shown by the dashed arrow which provides a momentum  $q'$ ); (iii) the electron/hole is scattered by a phonon with wavevector  $k_{(ZO')L}$ ; and (iv) electron–hole recombination. In  $k$ -space, the Dirac cones from top and bottom graphene layers (located at  $K_a$  and  $K_b$ ) are separated from each other by a distance that depends on the twisting angle  $\theta$  (see Figure 4a).<sup>4,10</sup> The larger the  $\theta$ , the more separated the  $K_a$  and  $K_b$  points, and thus more distant the two Dirac cones are. When  $\theta = \theta_c$  (see Figure 4d), the incident photon energy  $\hbar\omega_{in}$  equals the energy difference between the conduction and valence van Hove singularities.<sup>4,5</sup> Because tBLG maintains linear electronic dispersion of SLG, that is,  $E = \hbar v_F k$ , where the Fermi velocity  $v_F \approx 1 \times 10^6$  m/s and  $E = 2.33$  eV for a 532 nm photon, we can estimate the magnitude of the phonon wavevector  $k_{(ZO')L} = q' = 0.36$   $\text{\AA}^{-1}$  under 532 nm laser excitation. In this case, the magnitude of  $k_{(ZO')L}$  or  $q'$  is roughly half of the superlattice wavevector  $q$  and equals the distance between  $K_a$  and  $K_b$  (as shown in Figure 4a,d). The observed phonon frequency (94  $\text{cm}^{-1}$ ) and the phonon wavevector  $k_{(ZO')L}$  are in excellent agreement with the  $ZO'$  phonon dispersion in Bernal-stacked BLG (see the two uncircled points in Figure 5 for 532 and 633 nm laser excitations),<sup>23,27–29</sup> which confirms our assignment of this mode to the layer breathing mode ( $ZO'$ )<sub>L</sub>. It is worthwhile noting that momentum conservation in the Raman process is achieved through an intermediate step shown by the dashed

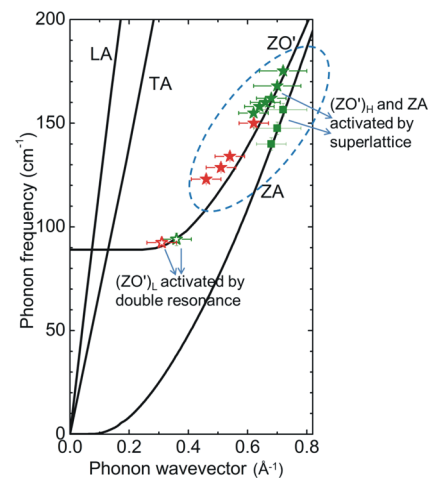


**Figure 5.** Low-frequency phonon dispersion. Different phonon branches are labeled. While the dispersion curves shown were calculated for SLG and Bernal-stacked bilayer graphene,<sup>13</sup> they are expected to be similar for tBLG for the relevant modes studied here. All points are determined by Raman measurements in this work. Points determined by a 532 nm laser excitation are shown in green, and those determined from a 633 nm laser excitation are shown in red.

arrow in Figure 4d. It is unlikely that this step is due to defect-induced scattering since the Raman intensity of the D band is reasonably weak in our samples (see the full Raman spectra in Figure 2a and in the Supporting Information). Therefore, this intermediate step is likely due to scattering of electrons by the tBLG crystal lattice, which lacks long-range periodicity (lattice translational symmetry).<sup>10,19</sup> This activation process is confirmed by the absence of the fundamental ( $ZO'$ )<sub>L</sub> mode Raman scattering from Bernal-stacked BLG that has long-range

lattice translational symmetries.<sup>15,23,30</sup> In Bernal-stacked BLG in which scattering due to tBLG crystal lattice is absent, the second-order ( $ZO'$ ) mode in which momentum conservation is satisfied by involving two  $ZO'$  phonons with opposite wavevectors, displays strong Raman intensity.<sup>15</sup> In addition, this  $(ZO')_L$  phonon in tBLG softens under 633 nm laser excitation (see Supporting Information), which further confirms that this phonon has a nonzero wavevector and that the scattering process can be explained by the double resonance mechanism.

When  $\theta < \theta_c$ , the two Dirac cones have substantial overlap. The Raman process accesses the overlapped area (involving both Dirac cones at locations  $K_a$  and  $K_b$ ) and allows phonons with wavevector  $k_{(ZO')_L}$  less than  $0.36 \text{ \AA}^{-1}$  to contribute to the Raman spectra (see Figure 4c). In this framework, the fwhm of this  $(ZO')_L$  mode will increase as  $\theta$  decreases (as the area of overlapped Dirac cones increases), which is supported by our observation shown in Figure 3b. In addition, the frequency of this  $(ZO')_L$  mode should reduce slightly as the twisting angle  $\theta$  decreases away from  $\theta_c$  as the overlapped Dirac cones enable  $(ZO')_L$  phonon with wavevector  $k_{(ZO')_L}$  less than  $0.36 \text{ \AA}^{-1}$  to contribute to the Raman spectra, which would lower the phonon energy (based on the  $ZO'$  phonon dispersion predicted in BLG<sup>23,27–29</sup>). Our observation of  $(ZO')_L$  phonon softening and broadening for  $\theta < \theta_c$  (see Figure 3a,b) confirms this interpretation and shows that the phonon wavevectors  $k_{(ZO')_L}$  (or  $q'$ ) is not uniquely defined by the twisting angle  $\theta$ . For  $\theta < \theta_c$ ,  $k_{(ZO')_L}$  and  $q'$  can have multiple values depending on the degree of overlap of the two Dirac cones (see Figure 4(c)). This is very different from the superlattice wavevector  $q$  that is solely determined by the twisting angle  $\theta$ .

For  $\theta > \theta_c$ , the Raman process does not access overlapped Dirac cones (see Figure 4(e)). Even if the area of Dirac cone overlap decreases as  $\theta$  increases, it should not affect the  $(ZO')_L$  phonon wavevector involved in the Raman process. This agrees well with our observation that the frequency and fwhm of the  $(ZO')_L$  mode remain unchanged when the twisting angle  $\theta$  is greater than  $\theta_c$ , as shown in Figure 3a,b. These results indicate that the  $(ZO')_L$  phonon is not very sensitive to the twisting of the two graphene layers for  $\theta \geq \theta_c$ . This feature of the  $(ZO')_L$  mode is very different from that of the  $(ZO')_H$  and other Raman modes, for example, R and R', whose frequencies vary monotonically with the twisting angle  $\theta$  and are sensitive to  $\theta$  for both  $\theta > \theta_c$  and  $\theta < \theta_c$ .<sup>13</sup> This difference indicates that the  $(ZO')_L$  mode does have a different Raman scattering mechanism from those phonons which are activated by the tBLG superlattice. The double resonance mechanism that we proposed above qualitatively explains the characteristics of the  $(ZO')_L$  mode as a function of  $\theta$ .

The tBLG system allows us to probe the dispersion of the layer breathing mode  $ZO'$  in a broad range off the Brillouin zone center (see Figure 5). Our measurements show that the dispersion of the  $ZO'$  mode in tBLG is similar to that of Bernal-stacked BLG,<sup>15</sup> which indicates that the interlayer out-of-plane vibrations of tBLG are comparable to those of Bernal-stacked BLG for  $\theta \sim \theta_c$ , consistent with the calculation shown in ref 31. The emergence of this fundamental layer breathing ( $ZO'$ ) vibration in the twisted BLG system (known to be silent in Bernal-stacked BLG and graphite<sup>14</sup>) implies that the crystal symmetry that makes the  $ZO'$  silent in Bernal-stacked BLG is lifted in tBLG.

Figure 3c displays the change of integrated intensity of the  $(ZO')_L$  mode as a function of normalized  $I_{2D}$  (and thus as a

function of  $\theta$ ). It is seen that the  $(ZO')_L$  mode intensity is strongly enhanced when the normalized  $I_{2D}$  is  $\sim 1.6$ , consistent with the critical value of 1.5 found in the changes in the frequency (Figure 3a) and fwhm (Figure 3b) of this mode. The normalized  $I_{2D}$  of  $\sim 1.6$  corresponds to a twisting angle  $\theta \approx 12.5^\circ$ , which agrees well with the value of  $\theta_c$ .<sup>5</sup> This observation indicates that the Raman intensity of the  $(ZO')_L$  phonon displays large resonance enhancement at  $\theta_c$ , where the intensity of the G Raman peak is also enhanced (see Figure 3e and refs 4 and 5). Our observation suggests that the  $(ZO')_L$  and the G modes share the same resonance enhancement mechanism arising from van Hove singularities in the DOS in the tBLG system.<sup>4,5</sup> The ratio of integrated intensities of the  $(ZO')_L$  and G peaks reaches a maximum value of  $\sim 7\%$  at resonance. It is very impressive that when  $\theta$  overlaps  $\theta_c$  the intensity of the  $(ZO')_L$  peak is comparable to that of the G band (off resonance), and that it is much stronger than the intensities of ZA,  $(ZO')_H$ , R, and R' peaks, as shown in Figure 2. This difference in resonance enhancement between the  $(ZO')_L$  and other modes further confirms that the Raman scattering mechanisms of these modes are different. The  $(ZO')_L$  mode that involves optical transitions between the conduction and valence van Hove singularities (see Figure 4d) are strongly enhanced, whereas the ZA,  $(ZO')_H$ , R, and R' modes due to superlattice scattering are not subject to the same enhancement. When  $\theta$  differs from  $\theta_c$  significantly ( $\theta < 10^\circ$  or  $> 15^\circ$ ), this  $(ZO')_L$  mode is not observed, likely due to its intensity becoming too weak to be detected.

Another striking feature of the  $\theta$ -dependent Raman spectra from tBLG is the large enhancement of the background intensity of low energy Raman modes at the critical twisting angle  $\theta_c$ . The background envelope on which the low-energy Raman lines superimpose (as highlighted by dashed lines in Figure 2b) is steepest for  $\theta \sim \theta_c$ . We define the height intensity of this background envelope at  $70 \text{ cm}^{-1}$  as the low-energy background intensity (as illustrated by the vertical arrow for the spectrum with  $\theta \sim 12^\circ$  in Figure 2a). Figure 3d shows the change of this low-energy background intensity as a function of the normalized  $I_{2D}$  (and thus as a function of  $\theta$ ). It is seen that this low-energy background intensity also reaches maximum at  $\theta_c$  (when the normalized  $I_{2D}$  is  $\sim 1.6$ ), similar to the resonance enhancements of the  $(ZO')_L$  and G Raman peaks. We speculate that this broad low-energy background envelope, which is strongly enhanced at the critical angle  $\theta_c$ , could be related to electronic excitations such as plasmons in tBLG.<sup>32,33</sup> Further investigations are needed to understand the origin of this enhanced low energy background.

Figure 2 shows that in addition to the two  $ZO'$  modes and ZA mode, an even lower energy mode around  $52 \text{ cm}^{-1}$  (X mode) is observed for  $\theta \sim \theta_c$ . This "X" mode appears to exhibit similar resonance enhancement as the  $(ZO')_L$  and G modes do near the critical twisting angle  $\theta_c$  and may be too weak to be seen when  $\theta$  is off  $\theta_c$ . Like the two  $ZO'$  modes, this X mode is also only observed in tBLG and is not observed in Bernal-stacked BLG.<sup>30</sup> On the other hand, previous experiments on Bernal-stacked BLG observed a shear mode (i.e., the C mode, occurring at  $\sim 31 \text{ cm}^{-1}$ ) that originates from the relative in-plane sliding of the two graphene layers.<sup>30</sup> An interlayer coupling strength of  $\sim 12.8 \times 10^{18} \text{ Nm}^{-3}$  is estimated from the position of the C mode in Bernal-stacked graphene layers.<sup>30</sup> In our measurements of tBLG, the rising background below  $50 \text{ cm}^{-1}$  (see Figure 2a,b) makes it very challenging to resolve and investigate the C mode (usually very weak in bilayer graphene)

in our samples. Hence, it is hard for us to estimate the interlayer coupling constant from the *C* mode of tBLG and compare it to that of Bernal-stacked graphene or graphite. The frequency of this *X* mode is much higher than that of the *ZA* mode with the phonon wavevector of  $\sim 0.36 \text{ \AA}^{-1}$  (see Figure 5). Therefore, the *X* mode cannot be assigned to a *ZA* phonon due to double resonance scattering, unlike the  $(\text{ZO}')_{\text{L}}$  mode. The exact nature of the *X* mode that we observe in tBLG is not yet clear at this time. We believe that the *X* mode is a different mode from the *C* mode since the position, line width, and line shape of the two modes are very different. The *C* mode in Bernal-stacked graphene has a narrow (a few  $\text{cm}^{-1}$  in width) asymmetric Fano line shape that results from quantum interference between a discrete phonon state and a relatively broad continuum of electronic or multiphonon transitions.<sup>30</sup> In contrast, the *X* and  $(\text{ZO}')_{\text{L}}$  modes in tBLG have larger fwhm ( $10\text{--}15 \text{ cm}^{-1}$ ) and Lorentzian lineshapes (see Figure 2), which are similar to those of the G Raman peak. This observation suggests that the *X* and  $(\text{ZO}')_{\text{L}}$  peaks are mainly influenced by the electron–phonon coupling, similar to what occurs for the G band.<sup>8,30</sup>

We suggest that one possible assignment for the *X* mode may be a torsional motion in which the top and bottom graphene layers execute out-of-phase rotations as schematically shown in Figure 4b. There will be multiple approximate symmetries for various twisting angles  $\theta$  ( $0^\circ \leq \theta \leq 30^\circ$ ), and the potential energy landscape should be characterized by small energy barriers between adjacent configurations, promoting low-energy torsional motions about a particular  $\theta$ .<sup>34</sup> Analogous low-energy motions are seen in  $\text{C}_{60}$ , where electron–phonon interactions give rise to low-energy torsional motions about distortion configurations.<sup>34</sup> In the tBLG system, the observed resonance enhancement of Raman scattering intensity from this torsion mode near  $\theta_c$  could result from electron–phonon coupling.

Such torsional modes in layered materials have received very little investigation so far. Studies of torsional modes in spherical materials such as nanoparticles have shown that if the shape of the particles is asymmetric due to deformation, torsional modes can be observed in low-frequency Raman scattering.<sup>35,36</sup> On the basis of this scenario, we speculate that the presence of a torsional mode in tBLG could be related to the lack of long-range translational symmetry in the system. The apparent absence of torsional modes in Bernal-stacked BLG may follow simply from the absence of rotations in the translational symmetry group: the energy cost of a small-angle rotation is greater than shear mode translations.<sup>34</sup>

Unlike the  $\text{ZO}'$  mode, which is an out-of-plane vibrational mode, the relative in-plane motion, such as the *C* mode and the torsional mode, of tBLG is expected to exhibit significant changes in comparison to that in Bernal-stacked graphene layers since tBLG has very little potential energy barrier to relative interlayer motion, as evidenced by superlubricity of rotated graphite<sup>37</sup> and multilayer graphene system.<sup>19</sup> The interlayer coupling in tBLG relevant for the *X* (torsion) mode could be linked to a restoring force that tends to rotate the twisted graphene layers to their natural stacking structures<sup>19</sup> and/or Moire periodic potentials formed in two rotated honeycomb lattices.<sup>25,38–40</sup> The presence of the *X* (torsion) mode and the fundamental layer breathing mode suggests that the two layers in tBLG do couple to each other, consistent with the existence of interlayer transport in tBLG.<sup>9,41,42</sup>

In summary, two Raman modes below  $100 \text{ cm}^{-1}$  previously unobserved in Bernal-stacked BLG are seen in tBLG when the

twisting angle is close to the critical angle at which the intensity of the G Raman peak is enhanced. The mode observed at  $\sim 94 \text{ cm}^{-1}$  (measured with a 532 nm laser) is assigned to the fundamental layer breathing mode  $(\text{ZO}')_{\text{L}}$ . The intensities of this  $(\text{ZO}')_{\text{L}}$  mode and the background envelope on which the low energy Raman lines superimpose display large resonance enhancements near the critical angle, concomitant with the large enhancement of the G Raman peak. The changes in position and line width of this mode as a function of twisting angle can be explained by the double resonance mechanism. It reveals the influence of angle-dependent electronic band overlaps on the Raman spectra. Another higher frequency mode  $(\text{ZO}')_{\text{H}}$  induced by superlattice modulation is also observed in Raman spectra simultaneously. The other low-energy Raman mode observed at  $\sim 52 \text{ cm}^{-1}$  is tentatively attributed to the torsion mode in which the two graphene layers rotate in the plane with respect to each other. It is worthwhile noting that although our proposed double resonance mechanism explains the Raman features of the  $(\text{ZO}')_{\text{L}}$  mode, there are two questions that remain open. One is the absence of the overtone  $2(\text{ZO}')_{\text{L}}$  mode (expected to occur at  $\sim 188 \text{ cm}^{-1}$ ) in the Raman spectra from tBLG (see Figure 2b,c). The second is why only the  $(\text{ZO}')_{\text{L}}$  line is observed yet no phonons from other branches are observed in the double resonance Raman process. We speculate that this could be linked to the nonzero electron–phonon matrix element of the  $\text{ZO}'$  vibration.<sup>28</sup> Further studies are required to understand the mechanism causing the absence of  $2(\text{ZO}')_{\text{L}}$  and other phonons within the double resonance framework in tBLG. A recent theoretical investigation has shown that phonon behaviors in tBLG are rather complex.<sup>43</sup> Our studies demonstrate that twisted bilayer graphene is a new system that exhibits fundamental properties that are distinct from those of Bernal-stacked bilayer graphene.

## ■ ASSOCIATED CONTENT

### 📄 Supporting Information

Details about sample preparation, Raman measurement conditions, AFM characterization of BLG domains, characterization of twisting angles, additional Raman characterizations of tBLG domains including the characterization of spectra excited by the 633 nm laser light, and Raman maps of the low-energy mode from a tBLG domain. This material is available free of charge via the Internet at <http://pubs.acs.org>.

## ■ AUTHOR INFORMATION

### Corresponding Author

\*E-mail: (R.H.) [rui.he@uni.edu](mailto:rui.he@uni.edu); (Y.P.C.) [yongchen@purdue.edu](mailto:yongchen@purdue.edu).

### Author Contributions

<sup>¶</sup>R.H. and T.-F.C. contributed equally to this work.

### Notes

The authors declare no competing financial interest.

## ■ ACKNOWLEDGMENTS

R.H. acknowledges support by a Provost's Pre-Tenure Summer Fellowship Award from the University of Northern Iowa. R.H. also acknowledges the donors of The American Chemical Society Petroleum Research Fund (Grant 53401-UNI10) for partial support of this research. C.D. acknowledges the support of a SOAR award made by UNI College of Humanities, Arts & Sciences. P.M.S. acknowledges support by NSF Grant DMR

1206530. J.M.B. acknowledges the support from National Science Foundation (ECCS-1240510 and DMR-0907336) and the Robert A Welch Foundation (E-1728). Y.P.C. thanks A. C. Ferrari and M.-Y. Chou for helpful discussion. Y.P.C. acknowledges partial supports from NSF, DTRA, and C. F. Day & Associates for the graphene synthesis and characterizations.

## REFERENCES

- (1) Ho, Y. H.; Wu, J. Y.; Chiu, Y. H.; Wang, J.; Lin, M. F. *Philos. Trans. R. Soc. London, Ser. A* **2010**, *368*, 5445–5458.
- (2) Novoselov, K. S.; McCann, E.; Morozov, S. V.; Fal'ko, V. I.; Katsnelson, M. I.; Zeitler, U.; Jiang, D.; Schedin, F.; Geim, A. K. *Nat. Phys.* **2006**, *2*, 177–180.
- (3) Zhang, Y. B.; Tang, T. T.; Girit, C.; Hao, Z.; Martin, M. C.; Zettl, A.; Crommie, M. F.; Shen, Y. R.; Wang, F. *Nature* **2009**, *459*, 820–823.
- (4) Kim, K.; Koh, S.; Tan, L. Z.; Regan, W.; Yuk, J. M.; Chatterjee, E.; Crommie, M. F.; Cohen, M. L.; Louie, S. G.; Zettl, A. *Phys. Rev. Lett.* **2012**, *108*, 246103.
- (5) Havener, R. W.; Zhuang, H. L.; Brown, L.; Hennig, R. G.; Park, J. *Nano Lett.* **2012**, *12*, 3162–3167.
- (6) Wang, Y. Y.; Ni, Z. H.; Liu, L.; Liu, Y. H.; Cong, C. X.; Yu, T.; Wang, X. J.; Shen, D. Z.; Shen, Z. X. *ACS Nano* **2010**, *4*, 4074–4080.
- (7) Robinson, J. T.; Schmucker, S. W.; Diaconescu, C. B.; Long, J. P.; Culbertson, J. C.; Ohta, T.; Friedman, A. L.; Beechem, T. E. *ACS Nano* **2013**, *7*, 637–644.
- (8) Yan, J.; Henriksen, E. A.; Kim, P.; Pinczuk, A. *Phys. Rev. Lett.* **2008**, *101*, 136804.
- (9) Perebeinos, V.; Tersoff, J.; Avouris, P. *Phys. Rev. Lett.* **2012**, *109*, 236604.
- (10) Carozo, V.; Almeida, C. M.; Ferreira, E. H. M.; Cancado, L. G.; Achete, C. A.; Jorio, A. *Nano Lett.* **2011**, *11*, 4527–4534.
- (11) Gupta, A. K.; Tang, Y. J.; Crespi, V. H.; Eklund, P. C. *Phys. Rev. B* **2010**, *82*, 241406.
- (12) Righi, A.; Costa, S. D.; Chacham, H.; Fantini, C.; Venezuela, P.; Magnuson, C.; Colombo, L.; Bacsá, W. S.; Ruoff, R. S.; Pimenta, M. A. *Phys. Rev. B* **2011**, *84*, 241409.
- (13) Campos-Delgado, J.; Caçado, L. G.; Achete, C. A.; Jorio, A.; Raskin, J.-P. *Nano Res.* **2013**, *6*, 269–274.
- (14) Ferrari, A. C.; Basko, D. M. *Nat. Nanotechnol.* **2013**, *8*, 235–46.
- (15) Lui, C. H.; Heinz, T. F. *Phys. Rev. B* **2013**, *87*, 121404.
- (16) Wu, W.; Jauregui, L. A.; Su, Z. H.; Liu, Z. H.; Bao, J. M.; Chen, Y. P.; Yu, Q. K. *Adv. Mater.* **2011**, *23*, 4898–4903.
- (17) Yu, Q. K.; Jauregui, L. A.; Wu, W.; Colby, R.; Tian, J. F.; Su, Z. H.; Cao, H. L.; Liu, Z. H.; Pandey, D.; Wei, D. G.; Chung, T. F.; Peng, P.; Guisinger, N. P.; Stach, E. A.; Bao, J. M.; Pei, S. S.; Chen, Y. P. *Nat. Mater.* **2011**, *10*, 443–449.
- (18) Wang, Y.; Su, Z.; Wu, W.; Nie, S.; Xie, N.; Gong, H.; Guo, Y.; Lee, J. H.; Xing, S.; Lu, X.; Wang, H.; Lu, X.; McCarty, K.; Pei, S.-S.; Robles-Hernandez, F.; Hadjiev, V. G.; Bao, J. *arXiv* **2013**, *1301*, 4488 <http://arxiv.org/abs/1301.4488>, (accessed Jan 18, 2013).
- (19) Brown, L.; Hovden, R.; Huang, P.; Wojcik, M.; Muller, D. A.; Park, J. *Nano Lett.* **2012**, *12*, 1609–1615.
- (20) Yan, K.; Peng, H. L.; Zhou, Y.; Li, H.; Liu, Z. F. *Nano Lett.* **2011**, *11*, 1106–1110.
- (21) Kalbac, M.; Frank, O.; Kong, J.; Sanchez-Yamagishi, J.; Watanabe, K.; Taniguchi, T.; Jarillo-Herrero, P.; Dresselhaus, M. S. *J. Phys. Chem. Lett.* **2012**, *3*, 796–799.
- (22) Araujo, P. T.; Mafra, D. L.; Sato, K.; Saito, R.; Kong, J.; Dresselhaus, M. S. *Sci. Rep.* **2012**, *2*, 1017.
- (23) Lui, C. H.; Malard, L. M.; Kim, S.; Lantz, G.; Laverge, F. E.; Saito, R.; Heinz, T. F. *Nano Lett.* **2012**, *12*, 5539–5544.
- (24) Das, A.; Pisana, S.; Chakraborty, B.; Piscanec, S.; Saha, S. K.; Waghmare, U. V.; Novoselov, K. S.; Krishnamurthy, H. R.; Geim, A. K.; Ferrari, A. C.; Sood, A. K. *Nat. Nanotechnol.* **2008**, *3*, 210–215.
- (25) He, R.; Zhao, L. Y.; Petrone, N.; Kim, K. S.; Roth, M.; Hone, J.; Kim, P.; Pasupathy, A.; Pinczuk, A. *Nano Lett.* **2012**, *12*, 2408–2413.
- (26) Huang, M. Y.; Yan, H. G.; Chen, C. Y.; Song, D. H.; Heinz, T. F.; Hone, J. *Proc. Natl. Acad. Sci. U.S.A.* **2009**, *106*, 7304–7308.
- (27) Borysenko, K. M.; Mullen, J. T.; Li, X.; Semenov, Y. G.; Zavada, J. M.; Nardelli, M. B.; Kim, K. W. *Phys. Rev. B* **2011**, *83*, 161402.
- (28) Sato, K.; Park, J. S.; Saito, R.; Cong, C. X.; Yu, T.; Lui, C. H.; Heinz, T. F.; Dresselhaus, G.; Dresselhaus, M. S. *Phys. Rev. B* **2011**, *84*, 035419.
- (29) Yan, J. A.; Ruan, W. Y.; Chou, M. Y. *Phys. Rev. B* **2008**, *77*, 125401.
- (30) Tan, P. H.; Han, W. P.; Zhao, W. J.; Wu, Z. H.; Chang, K.; Wang, H.; Wang, Y. F.; Bonini, N.; Marzari, N.; Pugno, N.; Savini, G.; Lombardo, A.; Ferrari, A. C. *Nat. Mater.* **2012**, *11*, 294–300.
- (31) Jiang, J. W.; Wang, B. S.; Rabczuk, T. *Appl. Phys. Lett.* **2012**, *101*, 023113.
- (32) Grigorenko, A. N.; Polini, M.; Novoselov, K. S. *Nat. Photonics* **2012**, *6*, 749–758.
- (33) Bostwick, A.; Speck, F.; Seyller, T.; Horn, K.; Polini, M.; Asgari, R.; MacDonald, A. H.; Rotenberg, E. *Science* **2010**, *328*, 999–1002.
- (34) Chancey, C. C.; O'Brien, M. C. M. *The Jahn-Teller Effect in C<sub>60</sub> and other Icosahedral Complexes*; Princeton University Press: Princeton, NJ, 1997.
- (35) Ovsyuk, N. N.; Novikov, V. N. *Phys. Rev. B* **1996**, *53*, 3113–3118.
- (36) Duval, E. *Phys. Rev. B* **1992**, *46*, 5795–5797.
- (37) Dienwiebel, M.; Verhoeven, G. S.; Pradeep, N.; Frenken, J. W. M.; Heimberg, J. A.; Zandbergen, H. W. *Phys. Rev. Lett.* **2004**, *92*, 126101.
- (38) Ohta, T.; Robinson, J. T.; Feibelman, P. J.; Bostwick, A.; Rotenberg, E.; Beechem, T. E. *Phys. Rev. Lett.* **2012**, *109*, 186807.
- (39) Bistrizter, R.; MacDonald, A. H. *Proc. Natl. Acad. Sci. U.S.A.* **2011**, *108*, 12233–12237.
- (40) Meng, L.; Chu, Z. D.; Zhang, Y. F.; Yang, J. Y.; Dou, R. F.; Nie, J. C.; He, L. *Phys. Rev. B* **2012**, *85*, 235453.
- (41) Lee, D. S.; Riedl, C.; Beringer, T.; Castro Neto, A. H.; von Klitzing, K.; Starke, U.; Smet, J. H. *Phys. Rev. Lett.* **2011**, *107*, 216602.
- (42) Morell, E. S.; Vargas, P.; Chico, L.; Brey, L. *Phys. Rev. B* **2011**, *84*, 195421.
- (43) Cocemasov, A. I.; Nika, D. L.; Balandin, A. A. *Phys. Rev. B* **2013**, *88*, 035428.